

Morphological expressions of crater infill collapse: model simulations of Chaotic Terrains on Mars

Manuel Roda,¹⁻²  George Marketos,²⁻³ Jan Westerweel,² and Rob Govers² 

Corresponding author: M. Roda, Universita' degli Studi di Milano, Dipartimento di Scienze della Terra, Via Mangiagalli, 34 - 20133 Milano, Italy (manuel.roda@unimi.it)

¹Universita' degli Studi di Milano,
Dipartimento di Scienze della Terra, Via
Mangiagalli, 34 - 20133 Milano, Italy

²Universiteit Utrecht, Faculty of
Geosciences, Heidelberglaan 2, 3584 CS
Utrecht, The Netherlands.

³currently at: Tony Gee and Partners
LLP, Hardy House, 140 High Street, Esher,
UK.

This article has been accepted for publication and undergone full peer review but has not been through the copyediting, typesetting, pagination and proofreading process which may lead to differences between this version and the Version of Record. Please cite this article as doi: 10.1002/2017GC006933

© 2017 American Geophysical Union
Received: Mar 22, 2017; Revised: Aug 29, 2017; Accepted: Aug 30, 2017

Abstract. Martian chaotic terrains are characterized by deeply depressed intensively fractured areas that contain a large number of low-strain tilted blocks. Stronger deformation (e.g. higher number of fractures) is generally observed in the rims when compared to the middle regions of the terrains. The distribution and number of fractures and tilted blocks are correlated with the size of the chaotic terrains. Smaller chaotic terrains are characterized by few fractures between undeformed blocks. Larger terrains show an elevated number of fractures uniformly distributed with single blocks. We investigate whether this surface morphology may be a consequence of the collapse of the infill of a crater. We perform numerical simulations with the Discrete Element Method and we evaluate the distribution of fractures within the crater and the influence of the crater size, infill thickness and collapsing depth on the final morphology. The comparison between model predictions and the morphology of the Martian chaotic terrains shows strong statistical similarities in terms of both number of fractures and correlation between fractures and crater diameters. No or very weak correlation is observed between fractures and the infill thickness or collapsing depth. The strong correspondence between model results and observations suggests that the collapse of an infill layer within a crater is a viable mechanism for the peculiar morphology of the martian chaotic terrains.

1. Introduction

Martian chaotic terrains show a peculiar morphology with no terrestrial analogue. They consist of deeply depressed areas (up to 4 km depth) characterized by randomly distributed fractures and isolated tilted blocks in between (Fig. 1) [Carr *et al.*, 1973; Sharp, 1973; Schultz and Orphal, 1978; Carr, 1980; Rotto and Tanaka, 1995; Chapman and Tanaka, 2002; Glotch and Christensen, 2005; Rodríguez *et al.*, 2005a, b; Meresse *et al.*, 2008; Roda *et al.*, 2014]. The chaotic terrains contain stronger deformation along their rims compared with the central regions. The central regions sometimes appear as rigid blocks with relatively few fractures (Fig. 1b and e). The distribution of fractures is related to the size of the chaotic terrains. Smaller ones show few fractures and some well detectable undeformed blocks concentrated in the central region (Fig. 1a,d and b,e). In contrast, larger ones show an elevated number of fractures with single blocks rather uniformly distributed along the entire chaotic region (Fig. 1c and f). Sometimes the blocks are not visible due to the intense deformation.

Roda *et al.* [2016], on the basis of statistical analysis of morphometric characteristics of chaotic terrains and floor fractured craters (such as diameter, amount of collapse and pristine depth) proposed the following sequence for formation of chaotic terrains. Initially a liquid lake formed within an impact crater. Low surface temperatures turned the lake into ice, which then got covered by infill sediments. The planetary heat flux together with the thermal insulation of sediments would have slowly melted the ice from below, and would have created a lake beneath the ice [Zegers *et al.*, 2010]. The ice layer would have become too thin to support the loads of the sediment on top, and a bottom load

from the volume decrease from the phase change from ice to water [Roda *et al.*, 2013]. Thermo-mechanical modeling of buried ice layers confirms that stable melting of the ice layer is possible for a broad range of Martian physical conditions [Zegers *et al.*, 2010; Roda *et al.*, 2013] and proceeds until the ice-water system is no more able to support the load of the infill layer which starts to collapse [Roda *et al.*, 2013]. The last step of the scenario (and the one that we investigate in this paper) would have been that failure and collapse of the ice would have caused the catastrophic expulsion of water from the lake into large surface channels and the chaotic terrain sediment morphology. [Zegers *et al.*, 2010; Roda *et al.*, 2013, 2014, 2016].

Here we test whether collapse of the crater-infill layer can result in the peculiar surface morphology shown by chaotic terrains. We perform numerical simulations of collapsing infill layers above craters of different sizes by using the Discrete Element Method (DEM). We test whether we can reproduce the highly depressed morphology and the peculiar distribution of fractures of the chaotic terrains, and we statistically evaluate the influence of the crater size, infill thickness and collapsing depth on the final morphology. Finally, we compare the model predictions with the statistical results for the Martian chaotic terrains.

2. Model strategy and setup

2.1. Method

The DEM, introduced by *Cundall* [1971] and extensively used to simulate the complex mechanical behaviour of materials (e.g. rocks, sands) that consists of individual grains or blocks, is used for this study. DEM has been used in the past to investigate collapse phenomena [e.g., *Holohan et al.*, 2011; *Bym et al.*, 2013; *Holohan et al.*, 2015]. *Bym et al.* [2013] show that DEM reproduces very well empirically-observed subsidence profiles, while

Holohan et al. [2011, 2015] show the evolution of fractures and stress during the collapse of a volcanic caldera because of the withdrawal of a magmatic body.

DEM is a time-stepping method in which the material is modelled as a collection of discrete particles (here discs) which interact with each other at their mutual contacts. Within each time-step forces between particles are calculated from current positions. These are then converted to accelerations for individual particles, which are integrated to calculate velocities and new particle positions. In this way individual particle deformations and internal forces within a material can be tracked in response to any prescribed boundary forces or displacements, and so the deformation mechanism resulting from a specific phenomenon can be investigated and visualised in great detail.

The contact behaviour is described by a force-displacement law (essentially a spring in both the directions normal and perpendicular to the contact plane). A frictional slider is also introduced in the tangential direction so as to limit the frictional force, and bonds (that can break when a specific stress is reached) can be installed at the contacts to model rock. In this study we use linear contact springs and the idea for the parallel bond [*Potyondy and Cundall*, 2004] which has been added to our version of the open-source programme LAMMPS [*Plimpton*, 1995; *Landry et al.*, 2003; *Bym et al.*, 2013] by *Marketos* [2013]. DEM input parameters for this study are given in Table 1, while the acceleration for gravity of Mars is used here (3.711 m/s^2). Kinetic energy is partially dissipated by damping the accelerations through the use of a local damping scheme with a coefficient of 0.7 [see *Cundall*, 1987].

2.2. Model setup

In order to reduce computational time (full 3D simulations would have required prohibitively large numbers of grains) we simplify the real three-dimensional problem into a 2D symmetric crater with appropriate boundary conditions (Fig. 2). Given the high degree of circularity of the chaotic terrains and floor fractured craters (e.g., Fig. 4 in *Roda et al.* [2016]) this approximation does not affect the morphology of fractures observed in the plane of the analysis. Three rigid boundaries (left, right and bottom) are used to define the computational domain (Fig. 2). Particles belonging to the crater rims are kept fixed in order to simulate the rigid area around the crater. The crater boundaries are overlain by horizontal layers of particles that represent the sedimentary infill (Fig. 2).

Most of the chaotic terrains have a diameter ranging between 20 and 120 km [*Roda et al.*, 2016]. Although some larger features exist (e.g. Aram Chaos, 250 km), part of them might have formed by overlapping impact craters [*Rodríguez et al.*, 2005a] or because of multiple processes [*Warner et al.*, 2011; *Rodríguez et al.*, 2011]. For this reason we simulate the collapse of an infill layer that overlies craters with 4 different widths: 30, 60, 120 and 240 km. The collapsed infill within the chaotic terrains precludes the direct measurement of depths and floor widths of the original pristine craters. Therefore the pristine depth used in the starting geometry is calculated here using diameter vs depth equations of *Boyce and Garbeil* [2007], *Robbins and Hynek* [2012] and *Tornabene et al.* [2013] and the floor diameter is calculated starting from its diameter according to the equation of *Pike* [1977] for crater larger than 20 km. On the basis of the minimum collapse measured for the chaotic terrains *Roda et al.* [2016], we select 4 possible infill thicknesses (1, 1.5, 2.25 and 3 km) to fill-up the craters as a function of their depth. However, we also test the option of

less infill within the craters by modelling half the thickness of the overburden layer (0.5, 0.75, 1.125 and 1.5 km respectively). A lower infill thickness than this is unlikely because of the low thermal insulation produced by sediments, that would preclude the ice melting from below [Zegers *et al.*, 2010; Schumacher and Zegers, 2011; Roda *et al.*, 2013]. Since the relationship between collapse and diameter of chaotic terrains we can observe on Mars refers to minimum values of collapse, we test the impact of higher collapsing depth on the resulting morphology. Simulations are summarized in Table 2.

The DEM sample is created through pluviation (raining under gravity) of the constituent particles into the rigid box formed by the crater walls. As particles are not monodisperse this creates a random packing in which the material fabric is representative of a sedimented material. No regular crystal planes which would have influenced fracture patterns within it are present. The number of particles in the DEM simulations ranges from 73,402 for the smallest crater up to 1,472,581 for the largest. Particle diameters are uniformly distributed between 20 and 30 m. This diameter range represents the smallest possible range to get a reasonable computation time while achieving sufficient detail in the material and allows for a good calibration of material properties with real ones (see Appendix A and B). The ratio of overburden thickness to average particle diameter ranges between 40 to 100. We verified that larger particles size does not significantly affect the final morphology models and the total number of fractures by running simulations with a particle size twice as large. The chosen particle size allows a good identification of discrete fractures as well as a satisfactory identification of strain gradients (Appendix B). An artificial plane is used during the setup of samples to support the load of the sediment cap after the removal of particles inside the crater. Particles subject to the weight of

particles above then compact until they reach a negligible kinetic energy, with the help of damping. The sample is now ready to start the simulation of the collapse which is initiated by removal of the supporting plane.

The sub-ice lake scenario of formation of chaotic terrains accounts for the occurrence of water capped by a thin ice layer that exists beneath the infill material before the collapse. After the breaking of the ice layer the overburden collapses and water rapidly escapes to the surface pushed by the load of the overlying material. Here we do not model the effects of the water and we simulate the collapse of sediments within a vacuum. The presence of water within the crater affects the rate of collapse only (i.e. the collapse proceeds slower) and not the deformation style. Recent model of fissure outflow from chaotic terrains [Marra *et al.*, 2014] predicts that the time required to empty the lake is on the order of tens of days, and an increase in size and number of fissures does not result in higher outflow discharges. Therefore, the pressure field in the water layer can be considered to be uniform through the entire collapsing process and no (or very small) pressure gradient is expected within the lake. Fractures propagate as the overburden collapses displacing the fluid below it, without being too heavily affected by its presence. Consequently, the resulting deformation style of the overburden layer would not be affected by presence of a water substratum, although the collapsing rate would be lower. Since all material properties in DEM model are instantaneous (i.e. they have no characteristic timescale), the deformation of the overburden layer does not depend on the velocity of the collapse and, in turn, on the occurrence of a water layer beneath.

The occurrence of clear and sharp fractures within the chaotic terrains and the high thermal inertia of the infill material suggest a rather rocky material with significant un-

confined strength. For these reasons we treat the overburden layer as rocky material. DEM input parameters are summarized in Table 1, and are the result of a calibration procedure described in Appendix A based on unconfined uniaxial compression tests [e.g., *Holohan et al.*, 2011]. The stress-strain curves for these tests (Appendix A) give elastic moduli and strength for the virtual rock mass of 26 GPa and 100 MPa respectively which are comparable to properties of basaltic rock mass material (5-50 GPa and 12-63 MPa respectively) obtained for planetary surfaces [*Schultz*, 1993].

Doubling the grain diameter does not result in a dramatic variation of the virtual rock mass parameters (Appendix B). Considering the few constraints and large uncertainties for martian rock parameters, this variation is fully acceptable. Variations in bond stiffness affect only the resulting Young's modulus of the virtual rock mass and do not affect the rock strength. Similarly, variations in the bond strength affect only the strength of the virtual rock mass leaving the Young's modulus unaffected (Appendix B).

3. Model results

Here we first consider the evolution of the deformation of the infill layer during the collapse within a crater and then we statistically analyze the final morphology in terms of fractures distribution and number in relation to crater size.

3.1. Evolution

During the collapse, the deformation of the overburden layer is similar to that of a clamped beam (see movie S1 in the Supporting Information for the animation of the collapse process). In this configuration the bottom is lengthened under tension and the top

is shortened under compression. Initially (Steps 0), the generated tensile and compressive stress is lower than the bond strength and no fractures occur (Fig. 3).

As collapse proceeds it is at the points of support of the overburden beam where stresses are largest and where cracks first nucleate (Fig. 3 - Steps 5-7). Then the deformation of the overburden layer moves inward nucleating new cracks (Fig. 3 - Steps 12). The coalescence of these cracks leads to increasing downwards flexure and stress redistribution which results in increased bending of the overburden beam and the development of cracks at its bottom. These are initially horizontal and then propagate up to the top surface at higher angles (Fig. 3 - Step 30). The final bending of the overburden layer progressively increases the aperture of the first rim fracture (F1), clearly separating the inner highly-deformed region from the less deformed peripheral region (Fig. 3 - Step 45).

This mechanism is rather symmetric on either side of the modelled crater (Fig. 4), but the location of faults is not exactly the same as a result of the randomness of the initial DEM material structure. The fracturing starts from the region close to the rim and progressively moves toward the center of the overburden layer (Fig. 4). The result of the collapse is a highly-fractured and deformed overburden layer made up of a number of small blocks. A single central block develops at the center of the crater (Fig. 4). The evolution of the collapse can be seen here to be similar even for larger craters (Figs 5, 6 and 7) with a progressive movement of fracturing from the rim towards the center of the crater.

Since the collapse is essentially a gravitational mechanism, the timescale of simulations is essentially instantaneous and varies as a function of the collapsing depth: the higher

the collapsing depth, the longer the collapse of the overburden, ranging from 200 to 350 seconds.

3.2. Final surface morphology

The final morphology is characterized by several tensile fractures and undeformed blocks in between (Fig. 4). High strain areas occur at the periphery of the crater while low strain blocks occur toward the center (Figs 8 and 9). The size of the crater has a strong influence on the final morphology. The larger the diameter of the crater the stronger the deformation affecting the overburden layer (Figs 5 to 7). For the largest crater, the deformation occurs intensively even in the central part of the overburden layer and no single central block is detectable (Figs 6 and 7). The generated blocks, although not very different in size, show a different distribution as a function of crater diameter. For a 30 km crater, the undeformed blocks are concentrated in the central region of the crater and high deformed zones characterize the periphery. For a 60 km crater, several undeformed blocks occur in the central region of the crater and only some blocks are present at the periphery. For 120 and 240 km craters, a rather uniform distribution of the undeformed blocks occurs from the central region to the periphery (Fig. 8). In all simulations, highly-deformed zones characterize the regions close to the rims and the number of fractures increases with the diameter of the crater (Figs 8 and 9).

In order to better define the amount of fractures characterizing the models and their influence of crater diameter, infill thickness and collapse depth, we analyze the final morphology of collapsed infill in all simulations. Fractures (blue) and low strain blocks are highlighted (red) in Figure 9 by different amount of accumulated shear strain (from 0 to 1). Therefore, we use a modular program for image data analysis (Gwyddion, *Nečas and*

Klapetek [2012]) to obtain the distribution of strain along a profile close to the surface of the collapsed infill. We evaluate this distribution in terms of strain roughness, such as the root mean square value of the strain magnitude over the evaluation profile. In particular we obtain the number of strain peaks along the crater floor that can be equated to fractures. We use a peak cut-off of 0.4 to distinguish between fractures (strain \geq 0.4) and deformed blocks (strain $<$ 0.4) on the basis of Figure 9. Higher values of the cut-off would preclude the detection of very high-strain areas that can be reasonably considered as fractures.

Strain roughness analysis shows that the amount of peaks of the final topography within the crater linearly increases with the diameter of the crater (Fig. 10a). We obtain a linear correlation between peaks and diameter with a slope of 0.38 and R^2 of 0.99. The analysis of variance (ANOVA) gives a meaningful correlation, expressed by a level of rejecting the correlation (Fisher parameter) of 0.004. We test the sensitivity of the correlation between number of fractures and crater diameter in case of lower overburden thickness and higher collapsing depth. The overburden thickness does not affect the relationship between the number of fractures and crater diameter (Fig. 10b), although the distribution of strain-free blocks is rather different (compare Fig.9a and Fig. 11a). We obtain a remarkably similar correlation with lower thickness of sediments, with a slope of 0.35 (compared to 0.38 of higher thickness), R^2 of 0.99 and a Fisher parameter of 0.006. The collapsing depth does not affect the simulation at all (Fig. 11) and higher collapse results in approximately the same number and distribution of fractures and strain-free blocks. We conclude that in the tested scenario the number of fractures and the final morphology of chaotic terrains is strongly affected by the diameter of the original crater.

4. Comparison with chaotic terrains morphology

Martian chaotic terrains are characterized by intensively fractured floor characterized by polygonal tilted blocks very different in size and separated by wide tensile faults [Carr *et al.*, 1973; Sharp, 1973; Carr, 1980; Schultz and Orphal, 1978; Kortenienmi, 2003; Kortenienmi *et al.*, 2006; Roda *et al.*, 2016]. Most of the chaotic terrains display stronger deformation at their rims compared to the central regions. The filling material along the rims are collapsed from the surrounding area and characterized by tensile fractures (Fig. 1). The orientations of the faults at the margins are vertical or gently inward-dipping, following the orientation of the crater rims. The orientation of fractures in the middle region of the chaos is not easily detectable because of the intense degradation of the fractures walls and sedimentation. The number and spacing of fractures is related to the size of the chaotic terrains (Fig. 1). Smaller chaotic terrains show few fractures and some well detectable undeformed blocks (Fig. 1a,b). In contrast, larger terrains show an elevated number of fractures with single blocks not always visible or rather uniformly distributed from the central region to the periphery (Fig. 1c).

There are therefore striking similarities between the morphology resulting from our model and that observed within the chaotic terrains (compare Fig. 1 with Figs 8 and 9). The number of fractures increases with the diameter of the crater and the deformation along the rims is well localized and intense, characterized by tensile fractures. For smaller craters (Figs 8a and 9a), single undeformed blocks are concentrated in the central region of the crater and high deformed zones characterized the periphery. For larger craters, a rather more uniform distribution of the undeformed blocks occurs from the central region to the periphery although higher damage is observed (Figs 8c,d and 9c,d).

In order to better constrain the relation between the number of fractures and the size of the crater we analyze the chaotic terrains of the database published by *Roda et al.* [2016]. For this dataset too, as for DEM results, we perform an image data analysis to get statistical information about the number of fractures characterizing the different chaotic terrains and we compare the observation with the model results. For each feature we obtain the roughness of infill topography, in terms of number of height of peaks along a prescribed topographic profile, by using Gwyddion software on DTM High Resolution Stereo Camera (HRSC) Mars images [*Jaumann et al.*, 2007] with spatial and vertical resolution of 10 m/pixel. In this case the peaks represent the depths of the negative topography, such as valleys, which are equated to fractures. The topography within the chaotic terrains can be strongly affected by the location of topographic profile, specially for small diameters (see for example Fig. 1a), resulting in a asymmetric distribution of valleys and peaks. To reduce the influence of profile location on the number of height of peaks the width of the evaluation profile is taken as large as possible, such as 128 pixels. Larger chaotic terrains instead, generally show a rather symmetric distribution of fractures (Fig. 1b and c) and the influence of profile location is negligible. Some chaotic terrains in the database of *Roda et al.* [2016] are not considered in the analysis due to lack of HRSC images coverage (Hydaspis 2, Auroae 1 and 2, Margatifer 2, Masurky, Timbuktu, Chryse 1, Aureum 6, Margatifer 5; see *Roda et al.* [2016] for location and references), or because their final morphology is thought to be the result of different or multiple processes operating within the same chaotic terrains (Oxia, Iamuna, Xanthe 1, Xanthe 2, Margatifer 6, Iani5, Hydraotes see database of *Roda et al.* [2016] for location and references).

We obtain the correlation between the number of peaks and the diameter of chaotic terrains and we compare it with the correlation obtained for the numerical simulations. The number of peaks within the chaotic terrains increases with the diameter (Fig. 9a) and the regression gives a linear correlation with a slope of 0.51 and R^2 of 0.67. The analysis of variance (ANOVA) gives a meaningful correlation expressed by a level of rejecting the correlation (Fisher parameter) of 0.001. The number of fractures obtained by the numerical simulations very well overlaps the number of fractures observed within the chaotic terrains for the same diameters (Fig. 9a) and the very small difference in the slope between the two correlations (model and observations) suggests a strong similarity in terms of number of fractures observed within the chaotic terrains and that predicted by the model of infill collapse. Since most part of the chaotic terrains ranges between 20 and 120 km we test the relationship between number of fractures and diameter excluding the outlier data (diameter >120 km, Fig. 10c). The analysis of variance (ANOVA) gives a meaningful correlation, with a Fisher parameter of 0.001, although the slope is higher (0.63) and R^2 is slightly lower 0.57. This still agrees with the model when the outliers are removed from the correlation. In fact we observe an increase in the correlation slope of the model from 0.38 to 0.44 with a R^2 still very high (0.99). The correlation remains strong, with a Fisher parameter of 0.08.

In the end, model predictions match the following observations on chaotic terrains: i) stronger deformation at the rims of the crater compared to the central regions; ii) the infill material along the rims is characterized by tensile fractures; iii) the orientations of the faults at the margins are vertical or gently inward-dipping, following the orientation of the crater rims; iv) smaller chaotic regions show few fractures and some well detectable

In order to better constrain the relation between the number of fractures and the size of the crater we analyze the chaotic terrains of the database published by *Roda et al.* [2016]. For this dataset too, as for DEM results, we perform an image data analysis to get statistical information about the number of fractures characterizing the different chaotic terrains and we compare the observation with the model results. For each feature we obtain the roughness of infill topography, in terms of number of height of peaks along a prescribed topographic profile, by using Gwyddion software on DTM High Resolution Stereo Camera (HRSC) Mars images [*Jaumann et al.*, 2007] with spatial and vertical resolution of 10 m/pixel. In this case the peaks represent the depths of the negative topography, such as valleys, which are equated to fractures. The topography within the chaotic terrains can be strongly affected by the location of topographic profile, specially for small diameters (see for example Fig. 1a), resulting in a asymmetric distribution of valleys and peaks. To reduce the influence of profile location on the number of height of peaks the width of the evaluation profile is taken as large as possible, such as 128 pixels. Larger chaotic terrains instead, generally show a rather symmetric distribution of fractures (Fig. 1b and c) and the influence of profile location is negligible. Some chaotic terrains in the database of *Roda et al.* [2016] are not considered in the analysis due to lack of HRSC images coverage (Hydaspis 2, Auroae 1 and 2, Margatifer 2, Masurky, Timbuktu, Chryse 1, Aureum 6, Margatifer 5; see *Roda et al.* [2016] for location and references), or because their final morphology is thought to be the result of different or multiple processes operating within the same chaotic terrains (Oxia, Iamuna, Xanthe 1, Xanthe 2, Margatifer 6, Iani5, Hydraotes see database of *Roda et al.* [2016] for location and references).

one. No or weak relation occurs between the final morphology of chaotic terrains and their overburden thickness and collapsing depth.

The simulated timescale of the collapse is almost instantaneous. We have no indication about the timescale of the process on Mars but, from models of fissure outflow from chaotic terrains [Marra *et al.*, 2014], we can estimate a time of tens of days to empty the lake. Furthermore, some hydrological analyses performed on outflow channels related to the chaotic terrains suggest that the water volume and formative timescale required to carve the channels is compatible with rapid (maximum tens of days) and catastrophic events [e.g. Baker, 2001; Pacifici *et al.*, 2009; Roda *et al.*, 2014; Rodriguez *et al.*, 2015]. The fast collapse of overburden layer and rapid water release suggested by sub-ice lake scenario agree with this interpretation. The timescale of collapse will be longer if water is considered beneath the overburden layer. Therefore, we can consider the modelled timescale as minimum possible timescale for the collapse.

We conclude that the collapse of an infill layer within a crater can reproduce the peculiar morphology of the chaotic terrains. Collapse constitutes the last phase of the buried sub-ice lake scenario. When we combine this conclusion with the positive tests of earlier phases of the scenario [Zegers *et al.*, 2010; Roda *et al.*, 2013, 2014, 2016], we conclude that the buried sub-ice lake scenario can be a viable scenario to explain the formation of martian chaotic terrains.

Appendix A: Material calibration

To calibrate the mechanical parameters of the simulations with those of natural rock mass we perform some unconfined uniaxial compression tests, following the procedure of Holohan *et al.* [2011]. A sample 2 km wide and 2 km thick (17,551 particles), ob-

tained through pluviation (raining under gravity) of the constituent particles within a rigid box, is compressed from the top and bottom using downward and upward moving plane respectively. The velocity is kept constant at 1 m/s. We compress the sample using different bond stiffnesses and strengths that reach up to the rupture (s2 in the Supporting Information). The obtain the normal stress - strain curves for the tests (Fig. 12).

The behaviour of the sample during the compression tests shows many characteristic aspects of real rock deformation, such as initial elasticity, followed by yielding, strain hardening, failure and strain softening. Young's modulus of the virtual rock mass is measured from the initial linear portions of such stress-strain curves and the peaks of the curves represent the strength of the virtual rock mass. These parameters are compared to those for real basaltic mass rock material obtained for planetary surfaces [*Schultz, 1993*] and widely used for Mars [e.g., *Musiol et al., 2011; Roda et al., 2013*]. The best similarity is obtained for a bond stiffness of 1.5×10^{10} N/m and bond strength of 100 MPa. The Young's modulus is perfectly in the natural range (5-50 GPa) while the strength is higher than natural ones (12-63 MPa) [*Schultz, 1993*]. However, we have to take into account that we are simulating a virtual rock mass with a mean grain size of 25 m, which largely affect the strength of the whole rock mass.

Appendix B: Sensitivity tests

We analyze the sensitivity of the model on three main input parameters that can affect the results: particle size, bond stiffness and bond strength. As already explained the value of the DEM input parameters could not be independently estimated and so we have to constrain these as function of the chosen particles size. However, unconfined uniaxial compression tests for particles diameter ranging between 37 and 62 m (average diameter

of 50 m) result in broadly similar stress - strain curves to the ones from tests with smaller particle sizes (compare Fig. 12 and Fig. 13a). For the same range of bond strengths (80, 100 and 200 MPa) the resulting virtual rock mass strength is a bit higher for larger particles diameter (Fig. 13a). The chosen virtual rock mass strength is attained with a bond strength of 100 MPa for particles size of 25 m and 80 MPa for a size of 50 m. These values are not very different and they are to the same order of magnitude. The Young's modulus is well reproduced for both particle sizes using the same bond strength. Therefore, a drastic change in the particles size does not result in a dramatic variation of the virtual rock mass parameters. Considering the few constraints and high uncertainties available for Mars rock parameters, this variation is fully acceptable.

Variations in bond stiffness affect the Young's modulus of the virtual rock mass and do not affect the rock strength. Similarly, variations in the bond strength affect the strength of the virtual rock mass leaving the Young's modulus unaffected (Fig. 13).

We evaluate the impact of different grain sizes on the final morphology of infill collapse within a crater. In Figure 14 the accumulated shear strain for 30 km crater and two particle sizes is represented. A smaller particle size allows a better definition of fractures along the entire crater and strain gradients. However for both simulations the localization of high strain areas along the rim of the crater with a broadly similar extension is evident. Furthermore the amount of fractures decreases from the periphery to the center of the crater in both cases. The good replication of the final surface morphology in the two simulations is also confirmed by the broadly similar number of peaks (reproducing the number of fractures) occurring along the crater and similar distribution of peaks as a function of the normalized height of the topographic profile (Fig. 15).

Acknowledgments. Netherlands Organization for Scientific Research (NWO) and Netherlands Space Office (NSO grant) are gratefully acknowledged. The open source code LAMMPS was used to perform the numerical simulations (<http://lammps.sandia.gov>), with few modifications. The open-source package Gwyddion [Nečas and Klapetek, 2012] was used to perform profile roughness analysis (<http://gwyddion.net/>). We gratefully acknowledge the editor Thorsten Becker, Edwin Kite and the anonymous reviewer for their highly constructive criticism of the text.

References

- Baker, V. R. (2001), Water and the martian landscape, *Nature*, *412*(6843), 228–236.
- Boyce, J. M., and H. Garbeil (2007), Geometric relationships of pristine Martian complex impact craters, and their implications to Mars geologic history, *Geophysical Research Letters*, *34*(16), 1–5, doi:10.1029/2007GL029731.
- Bym, T., G. Marketos, J. Burland, and C. O’Sullivan (2013), Use of a two-dimensional discrete-element line-sink model to gain insight into tunnelling-induced deformations, *Géotechnique*, *63*(9), 791–795, doi:10.1680/geot.12.T.003.
- Carr, M. H. (1980), Morphology of the martian surface, *Space Science Reviews*, *25*(3), 231–284.
- Carr, M. H., H. Masursky, and R. S. Saunders (1973), A generalized geologic map of Mars, *Journal of Geophysical Research*, *78*(20), 4031–4036, doi:10.1029/JB078i020p04031.
- Chapman, M. G., and K. L. Tanaka (2002), Related magma-ice interactions: Possible origins of chasmata, chaos, and surface materials in Xanthe, Margaritifer, and Meridiani Terrae, Mars, *Icarus*, *155*(2), 324–339, doi:10.1006/icar.2001.6735.

- Cundall, P. A. (1971), A computer model for simulating progressive large scale movements in blocky rock systems, in *Proceedings of the Symposium of International Society of Rock Mechanics. Nancy, France*, vol. 1, pp. II–8.
- Cundall, P. A. (1987), Distinct element models for rock and soil structure, in *Analytical and Computational Methods in Engineering Rock Mechanics*, edited by E. T. Brown, pp. 129–163, George Allen and Unwin ltd, London.
- Glotch, T. D., and P. R. Christensen (2005), Geologic and mineralogic mapping of Aram Chaos: evidence for a water-rich history, *Journal of Geophysical Research*, *110*, E09,006, doi:10.1029/2004JE002389.
- Holohan, E. P., M. P. J. Schöpfer, and J. J. Walsh (2015), Stress evolution during caldera collapse, *Earth and Planetary Science Letters*, *421*, 139 – 151, doi: <http://dx.doi.org/10.1016/j.epsl.2015.03.003>.
- Holohan, E. P., M. P. J. Schöpfer, and J. J. Walsh (2011), Mechanical and geometric controls on the structural evolution of pit crater and caldera subsidence, *Journal of Geophysical Research: Solid Earth*, *116*(B7), 1–23, doi:10.1029/2010JB008032.
- Jaumann, R., G. Neukum, T. Behnke, T. C. Duxbury, K. Eichentopf, J. Flohrer, S. Gasselt, B. Giese, K. Gwinner, E. Hauber, H. Hoffmann, A. Hoffmeister, U. Köhler, K.-D. Matz, T. B. McCord, V. Mertens, J. Oberst, R. Pischel, D. Reiss, E. Ress, T. Roatsch, P. Saiger, F. Scholten, G. Schwarz, K. Stephan, and M. Wählisch (2007), The high-resolution stereo camera (HRSC) experiment on Mars Express: Instrument aspects and experiment conduct from interplanetary cruise through the nominal mission, *Planetary and Space Science*, *55*(7–8), 928–952, doi:10.1016/j.pss.2006.12.003.

- Korteniemi, J. (2003), Collapses and depressions post-dating crater formation in Martian impact structures – distribution and consequences, in *rd International Conference on Large Meteorite Impacts, Nördlingen, Germany*, p. 4091.
- Korteniemi, J., M. Aittola, T. Öhman, and J. Raitala (2006), Floor-fractured craters on the terrestrial planets – The martian perspective, in *proceedings of the first International Conference on Impact Cratering in the Solar System*, edited by A. Wilson, p. 2145, ESA Publications Division, Noordwijk, The Netherlands.
- Landry, J. W., G. S. Grest, L. E. Silbert, and S. J. Plimpton (2003), Confined granular packings: Structure, stress, and forces, *Physical Review E*, *67*(4), 1–9, doi:10.1103/PhysRevE.67.041303.
- Marketos, G. (2013), *Opening up High Performance Computing to the Discrete Element Method User Community*, UK National Supercomputing Service.
- Marra, W. A., E. Hauber, S. J. McLelland, B. J. Murphy, D. R. Parsons, S. J. Conway, M. Roda, R. Govers, and M. G. Kleinhans (2014), Pressurized groundwater outflow experiments and numerical modeling for outflow channels on Mars, *Journal of Geophysical Research E: Planets*, *119*(12), 2668–2693, doi:10.1002/2014JE004701.
- Meresse, S., F. Costard, N. Mangold, P. Masson, and G. Neukum (2008), Formation and evolution of the chaotic terrains by subsidence and magmatism: Hydraotes Chaos, Mars, *Icarus*, *194*(2), 487–500, doi:10.1016/j.icarus.2007.10.023.
- Musiol, S., B. Cailleau, T. Platz, T. Kneissl, A. Dumke, and G. Neukum (2011), Outflow activity near Hadriaca Patera, Mars: Fluid-tectonic interaction investigated with High Resolution Stereo Camera stereo data and finite element modeling, *Journal of Geophysical Research*, *116*(E8), doi:10.1029/2010JE003791.

- Nečas, D., and P. Klapetek (2012), Gwyddion: an open-source software for SPM data analysis, *Open Physics*, *10*(1), 181, doi:10.2478/s11534-011-0096-2.
- Pacifici, A., G. Komatsu, and M. Pondrelli (2009), Geological evolution of Ares Vallis on Mars: Formation by multiple events of catastrophic flooding, glacial and periglacial processes, *Icarus*, *202*(1), 60–77, doi:10.1016/j.icarus.2009.02.029.
- Pike, R. J. (1977), Size-dependence in the shape of fresh impact craters on the moon, in *Impact and Explosion Cratering*, Pergamon Press, New York.
- Plimpton, S. (1995), Fast Parallel Algorithms for Short-Range Molecular Dynamics, *Journal of Computational Physics*, *117*, 1–19.
- Potyondy, D. O., and P. A. Cundall (2004), A bonded-particle model for rock, *International Journal of Rock Mechanics and Mining Sciences*, *41*(8), 1329–1364, doi: <http://dx.doi.org/10.1016/j.ijrmms.2004.09.011>.
- Robbins, S. J., and B. M. Hynek (2012), A new global database of Mars impact craters ≥ 1 km: 2. Global crater properties and regional variations of the simple-to-complex transition diameter, *Journal of Geophysical Research: Planets*, *117*(E6), 1–21, doi: 10.1029/2011JE003967.
- Roda, M., R. Govers, and T. E. Zegers (2013), Melting and mechanical stability of sub-ice lake: a possible scenario for Aram Chaos evolution (Mars), *Rendiconti online della Società Geologica Italiana*, *129*, 146–149.
- Roda, M., M. G. Kleinhans, T. E. Zegers, and J. H. P. Oosthoek (2014), Catastrophic ice lake collapse in Aram Chaos, Mars, *Icarus*, *236*, 104–121, doi: 10.1016/j.icarus.2014.03.023.

- Roda, M., M. G. Kleinhans, T. E. Zegers, and R. Govers (2016), Origin of circular collapsed landforms in the Chryse region of Mars, *Icarus*, *265*, 70–78, doi:10.1016/j.icarus.2015.10.020.
- Rodríguez, J. A. P., S. Sasaki, R. O. Kuzmin, J. M. Dohm, K. L. Tanaka, H. Miyamoto, K. Kurita, G. Komatsu, A. G. Fairen, and J. C. Ferris (2005a), Outflow channel sources, reactivation, and chaos formation, Xanthe Terra, Mars, *Icarus*, *175*(1), 37–57, doi:10.1016/j.icarus.2004.10.025.
- Rodríguez, J. A. P., S. Sasaki, J. M. Dohm, K. L. Tanaka, B. Strom, J. Kargel, R. O. Kuzmin, H. Miyamoto, J. G. Spray, A. G. Fairen, G. Komatsu, K. Kurita, and V. R. Baker (2005b), Control of impact crater fracture systems on subsurface hydrology, ground subsidence, and collapse, Mars, *Journal of Geophysical Research-Planets*, *110*(E6), 1–22, doi:10.1029/2004JE002365.
- Rodríguez, J. A. P., J. S. Kargel, K. L. Tanaka, D. A. Crown, D. C. Berman, A. G. Fairén, V. R. Baker, R. Furfaro, P. Candelaria, and S. Sasaki (2011), Secondary chaotic terrain formation in the higher outflow channels of southern circum-Chryse, Mars, *Icarus*, *213*(1), 150–194, doi:10.1016/j.icarus.2010.09.027.
- Rodríguez, J. A. P., J. S. Kargel, V. R. Baker, V. C. Gulick, D. C. Berman, A. G. Fairén, R. Linares, M. Zarroca, J. Yan, H. Miyamoto, and N. Glines (2015), Martian outflow channels: How did their source aquifers form, and why did they drain so rapidly?, *Scientific Reports*, *5*, 13,404.
- Rotto, S., and K. L. Tanaka (1995), Geologic/geomorphic map of the Chryse Planitia Region of Mars (1:5,000,000), in *Miscellaneous Investigations Series Map. Department of the Interior*, United States Geological Survey.

- Schultz, P. H., and D. L. Orphal (1978), Floor-fractured craters on the Moon and Mars, *Meteoritics*, *13*, 622–625.
- Schultz, R. A. (1993), Brittle strength of basaltic rock masses with applications to venus, *Journal of Geophysical Research: Planets*, *98*(E6), 10,883–10,895, doi:10.1029/93JE00691.
- Schumacher, S., and T. E. Zegers (2011), Aram Chaos and its constraints on the surface heat flux of Mars, *Icarus*, *211*(1), 305–315, doi:10.1016/j.icarus.2010.09.023.
- Sharp, R. P. (1973), Mars - Fretted and chaotic terrains, *Journal of Geophysical Research*, *78*(20), 4073–4083.
- Tornabene, L. L., V. Ling, G. R. Osinski, J. M. Boyce, T. N. Harrison, and A. S. McEwen (2013), A revised global depth-diameter scaling relationship for Mars based on pitted impact melt-bearing craters, in *44th Lunar and Planetary Science Conference, The Woodlands, Texas*, p. 2592.
- Warner, N. H., S. Gupta, J.-R. Kim, J.-P. Muller, L. Le Corre, J. Morley, S.-Y. Lin, and C. McGonigle (2011), Constraints on the origin and evolution of Iani Chaos, Mars, *Journal of Geophysical Research*, *116*(E6), 1–29, doi:10.1029/2010JE003787.
- Zegers, T. E., J. H. P. Oosthoek, A. P. Rossi, J. K. Blom, and S. Schumacher (2010), Melt and collapse of buried water ice: An alternative hypothesis for the formation of chaotic terrains on Mars, *Earth and Planetary Science Letters*, *297*(3–4), 496–504, doi:10.1016/j.epsl.2010.06.049.

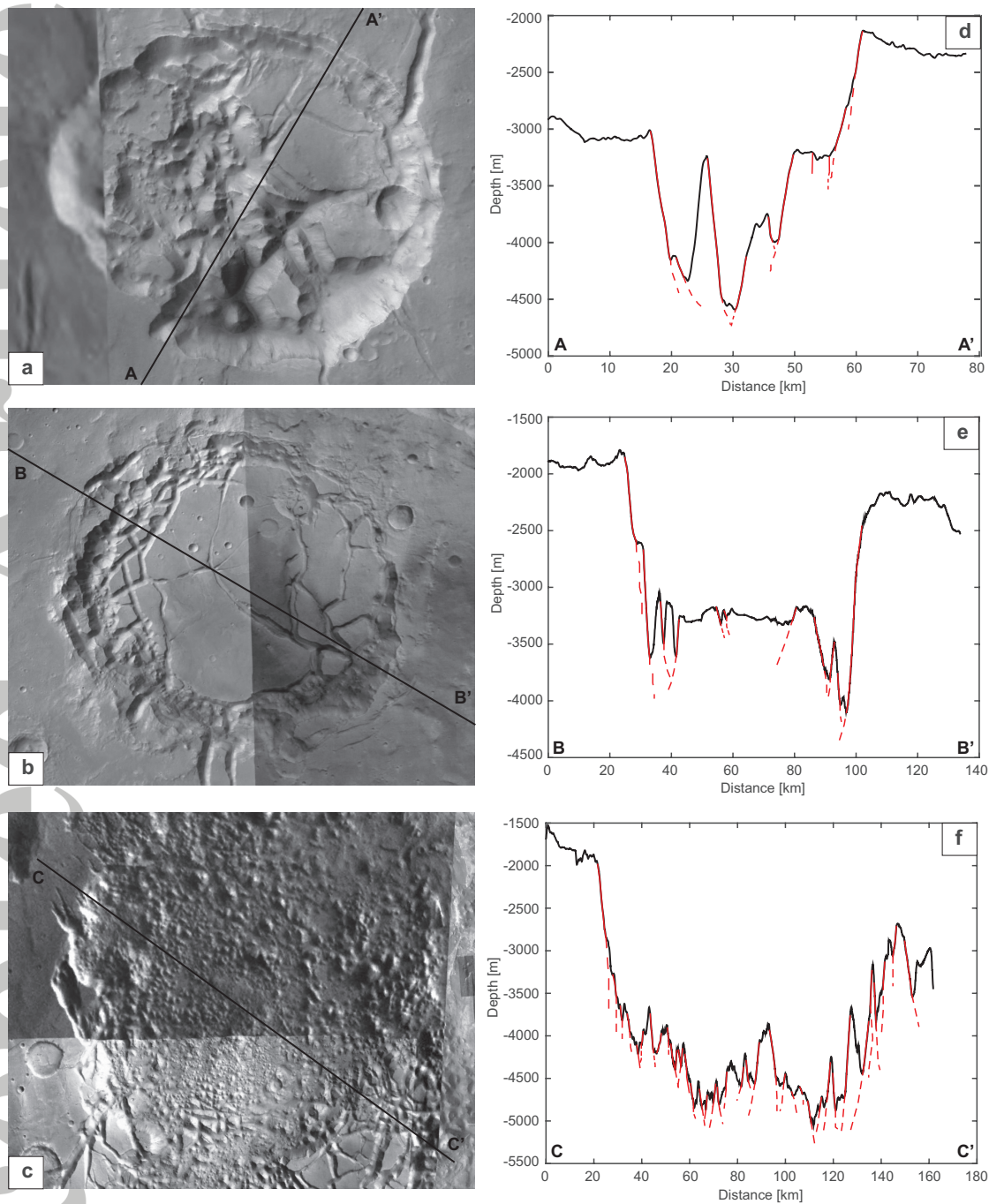


Figure 1. Three examples of martian chaotic terrains as a function of different diameter (a, b and c) and relative cross sections (d, e and f). In the cross sections, black lines represent the crater topography and red lines represent effective (solid) and interpreted (dashed) fractures. 30 km chaos (coordinates: $0^{\circ}28' N$, $28^{\circ}35' W$), 60 km chaos (coordinates: $0^{\circ}08' S$, $22^{\circ}46' W$) and 120 km chaos (coordinates: $4^{\circ}37' S$, $28^{\circ}22' W$). High Resolution Stereo Camera (HRSC) Mars images [Jaumann *et al.*, 2007].

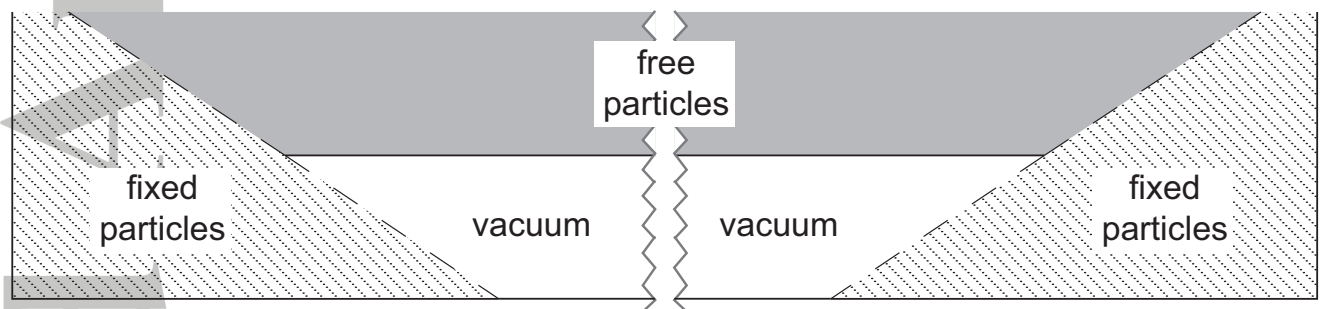


Figure 2. Model setup. Particles belonging to the overburden are mechanically free while those belonging to the crater are fixed. External walls of the domain (left, right and bottom) are frictionless. An empty crater is considered. Initially, an artificial horizontal plane is used to support the load of the infill. The plane is removed when the simulation starts and the infill layer is allowed to collapse. Solid lines represent effective walls, dashed line represents particles boundaries. Not to scale.

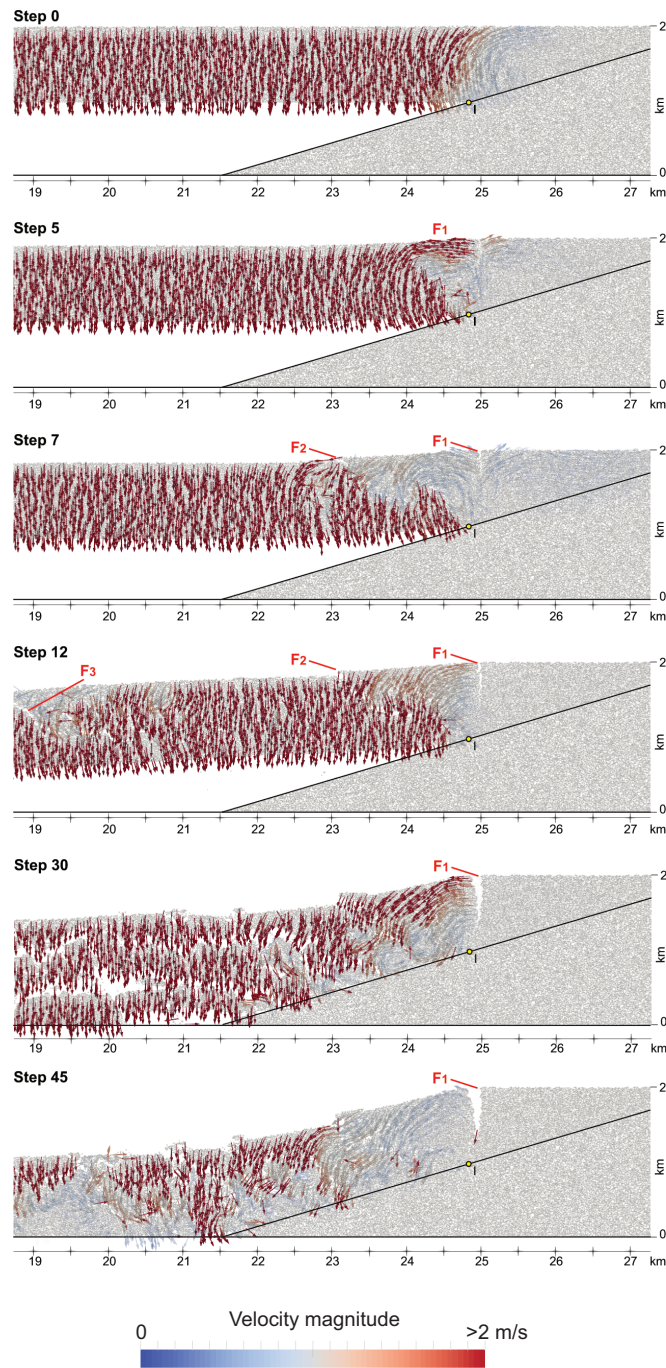


Figure 3. Velocity field on the right side for the simulation with a crater diameter of 30 km for different steps. Yellow point (I) represents the intersection between the overburden layer and the rim of the crater (black lines). Three different generations of faults are indicated with red letters. Downward acceleration occurs with the proceeding of the collapse. The first fault occurs above the I point and it is vertical. The other generations of fractures progressively nucleate inward as the proceeding of the collapse and they develop as outward-dipping faults. Several faults and blocks are predicted at the end of the collapse process. Vectors length is constant and

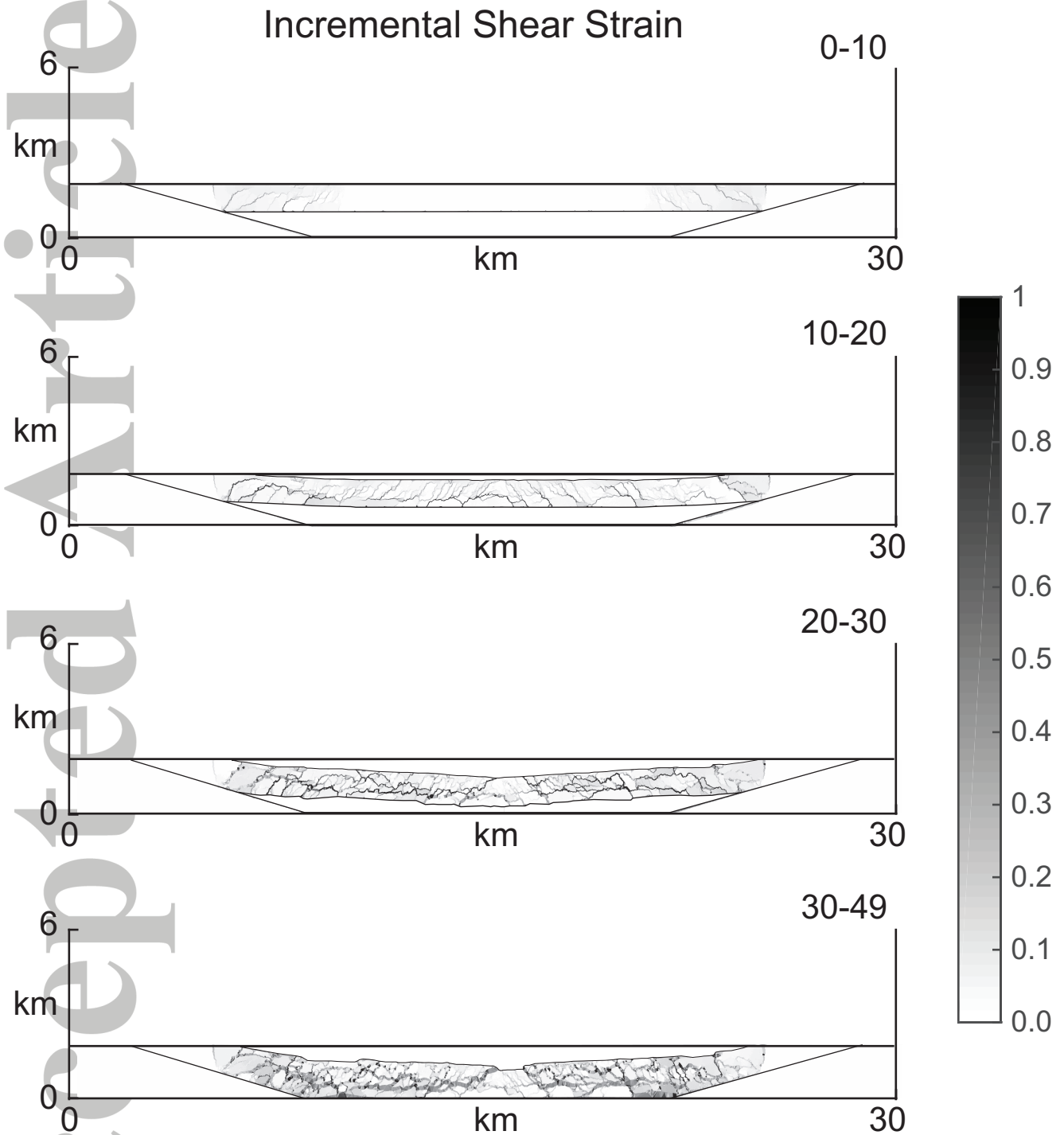


Figure 4. Incremental shear strain accumulated (from 0 to 1 represented by the grey scale) by a collapse of a crater diameter of 30 km at 4 different step ranges. Black lines represent crater rims and topography. The collapse process is rather symmetric. The fracturing starts from the region close to the rim and moves progressively to the center of the overburden layer. The result of the collapse is an highly fractured and deformed infill layer characterized by several small blocks. One single central block develops at the central region of the crater.

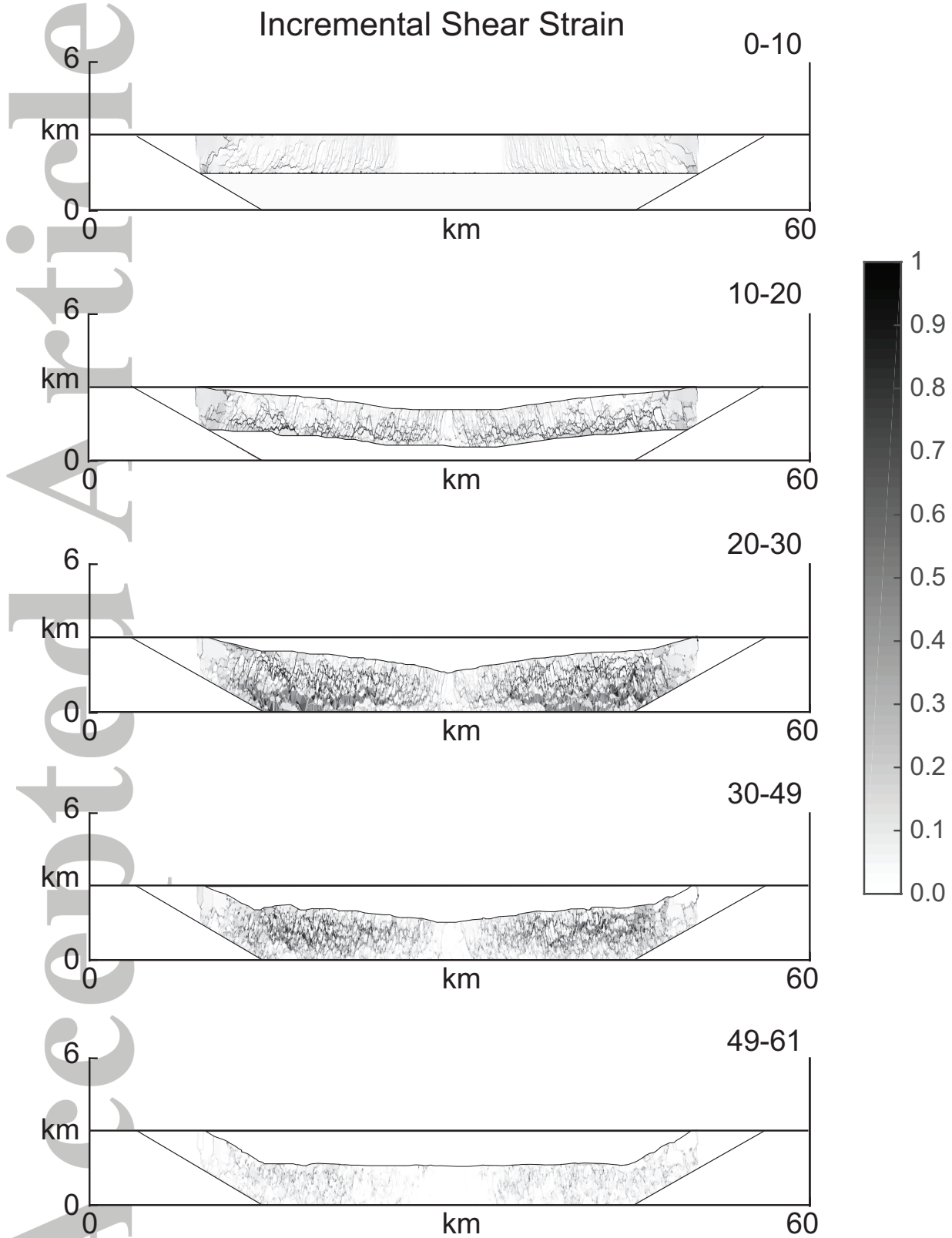


Figure 5. Incremental shear strain accumulated by a collapse a crater diameter of 60 km at 5 different step ranges.

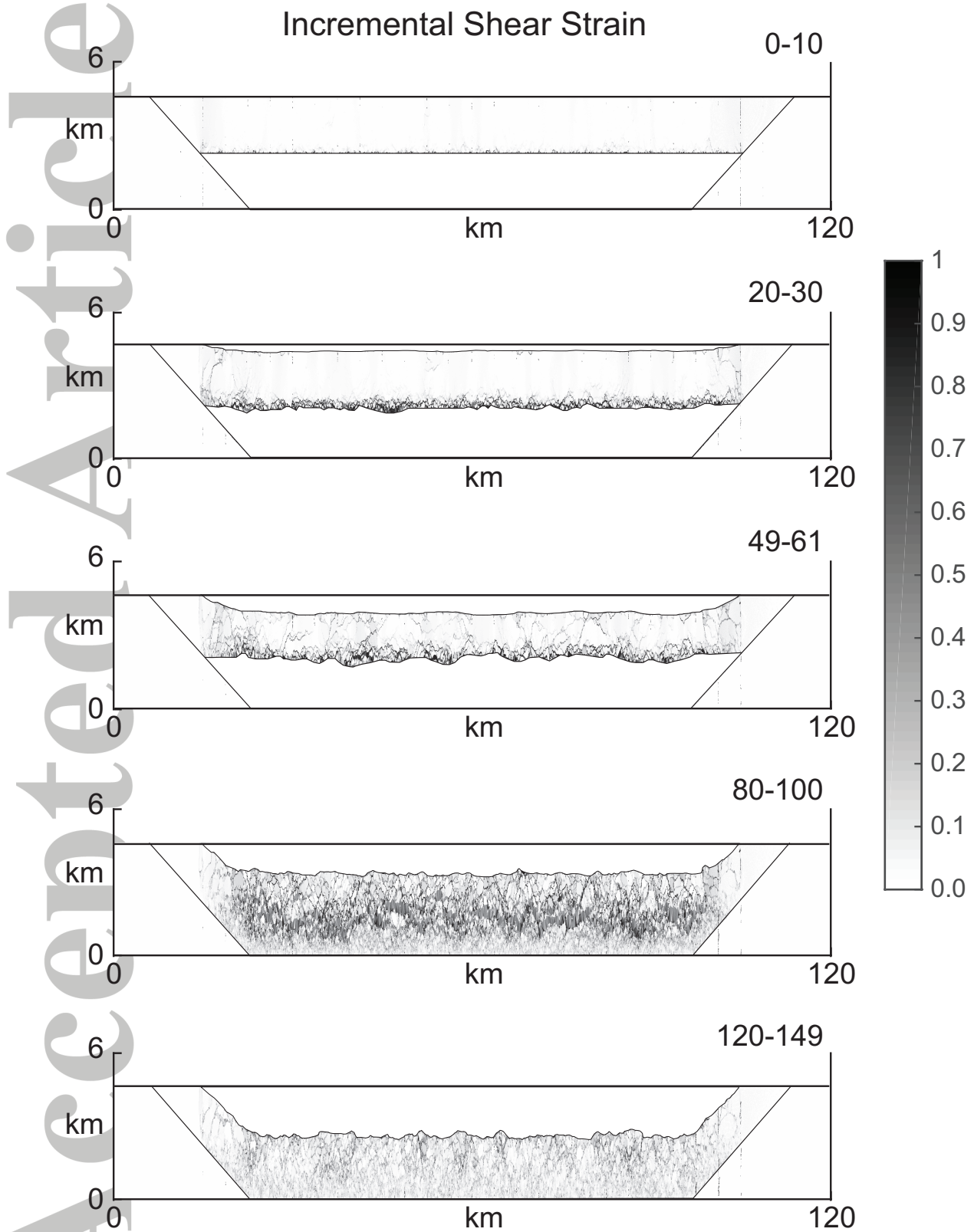


Figure 6. Incremental shear strain accumulated by a collapse a crater diameter of 120 km at 5 different step ranges.

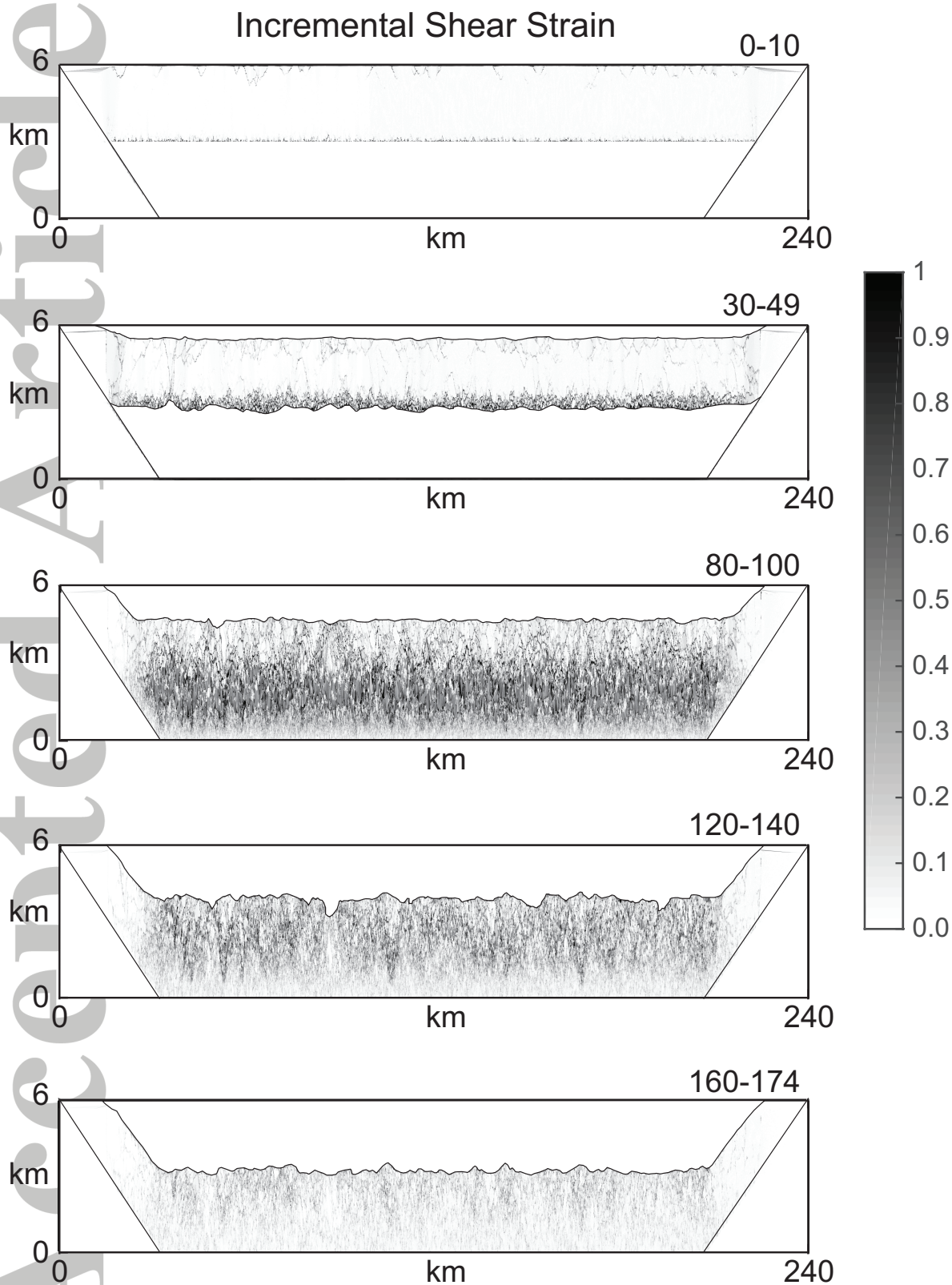


Figure 7. Incremental shear strain accumulated by a collapse a crater diameter of 240 km at 5 different step ranges.

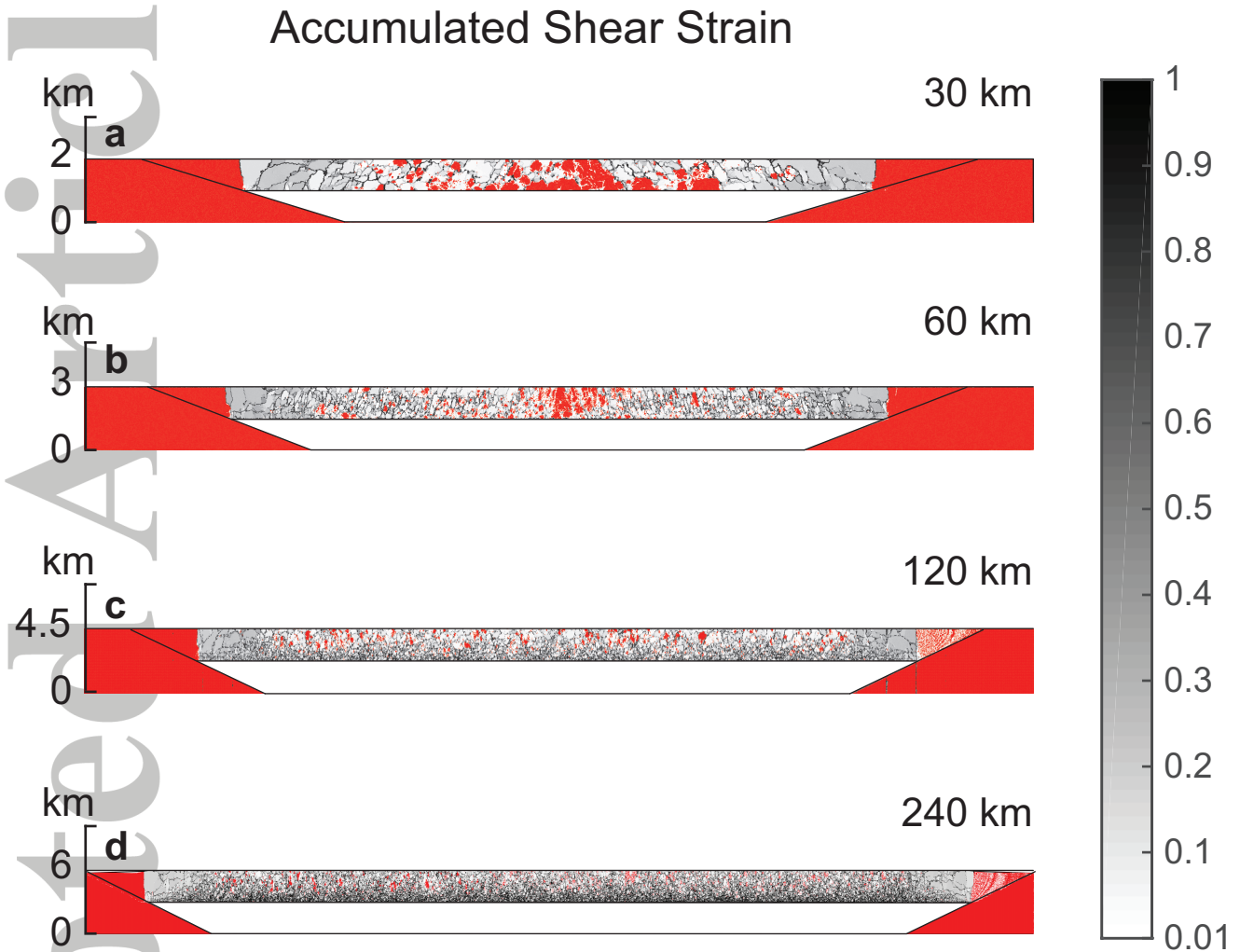


Figure 8. Total accumulated shear strain for crater diameters of (a) 30, (b) 60, (c) 120 and (d) 240 km. Grey areas represent the amount of accumulated strain. Red areas represent strain-free regions interpreted as undeformed blocks. For 30 km crater the undeformed blocks are concentrated in the center of the crater and high deformed zones characterized the periphery. For 60 km crater several undeformed blocks occur in the central region of the crater and only some blocks are present at the periphery. For 120 and 240 km crater a rather uniform distribution of the undeformed blocks occurs.

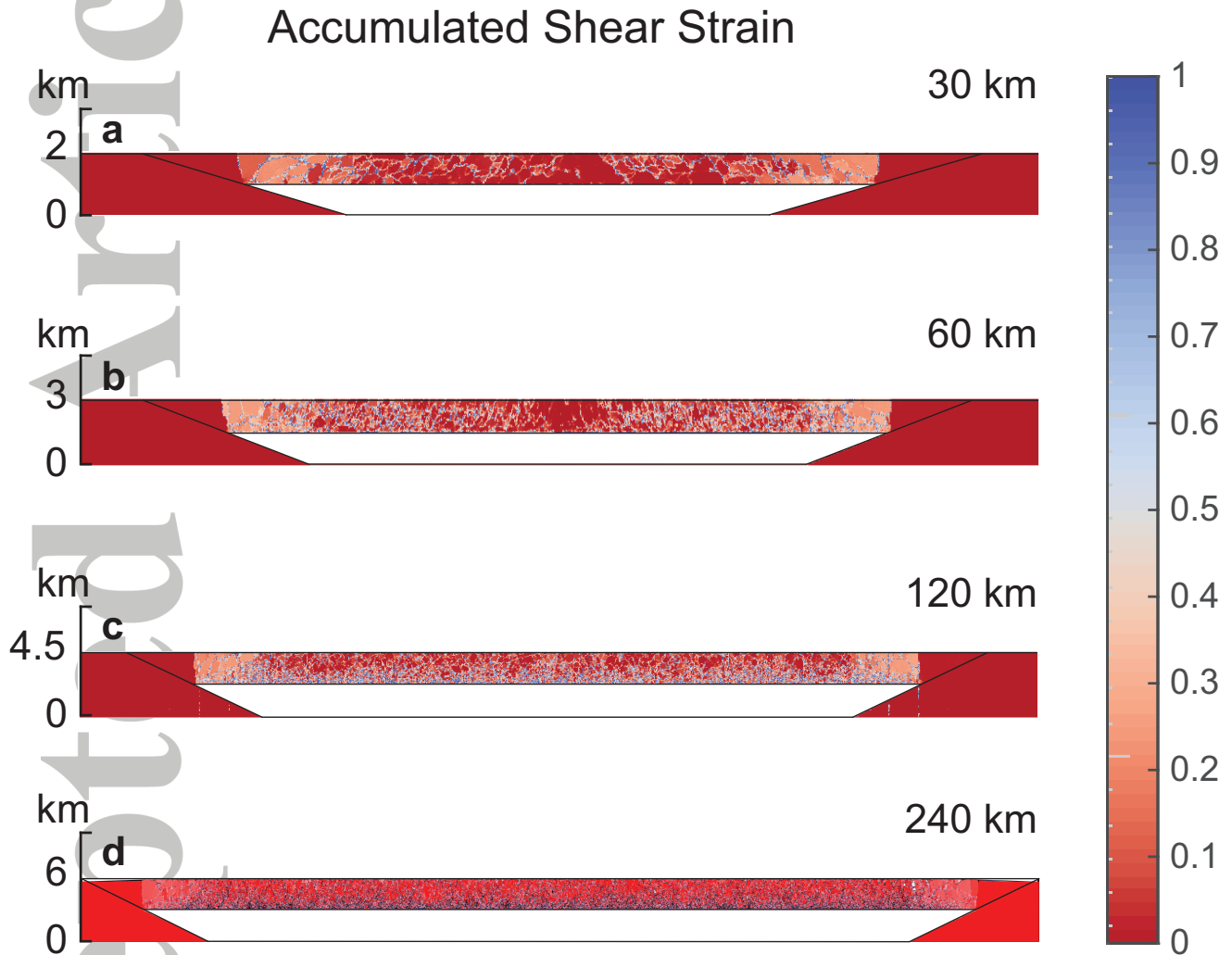


Figure 9. Total accumulated shear strain for crater diameters of (a) 30, (b) 60, (c) 120 and (d) 240 km. Light red and blue areas represent regions with a very high strain (≥ 0.4) interpreted as fractures. In all simulations a high deformed zone characterizes the region close to the rims of the crater and the number of fractures generated increases with the diameter of the crater.

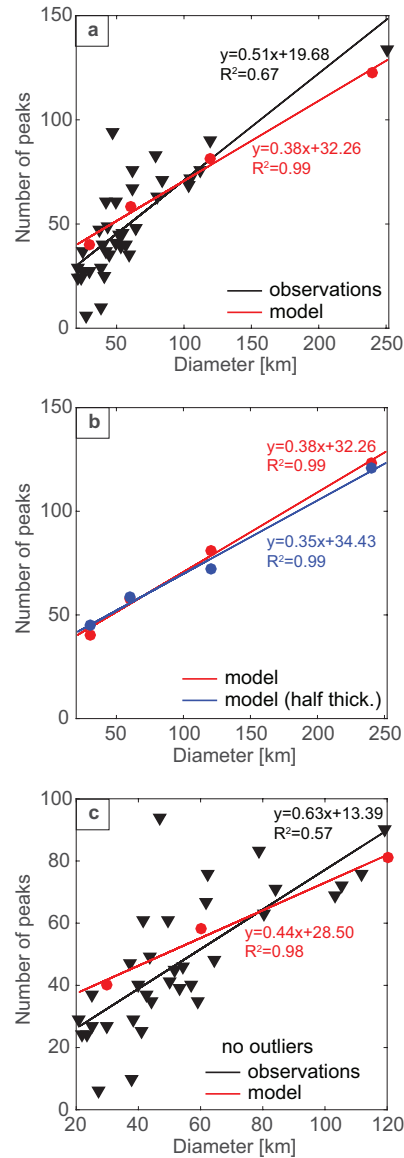


Figure 10. a) Statistical correlations between diameter of craters and number of fractures (peaks) of the final infill morphology for the numerical simulations (red) and the chaotic terrains (black). Regression equations and R^2 are also reported. b) Statistical correlations between diameter of craters and number of fractures for the numerical simulations with different overburden thickness: red - normal thickness; blue - half thickness. c) Statistical correlations between diameter of craters and number of fractures for the numerical simulations (red) and the chaotic terrains (black) excluding outliers data.

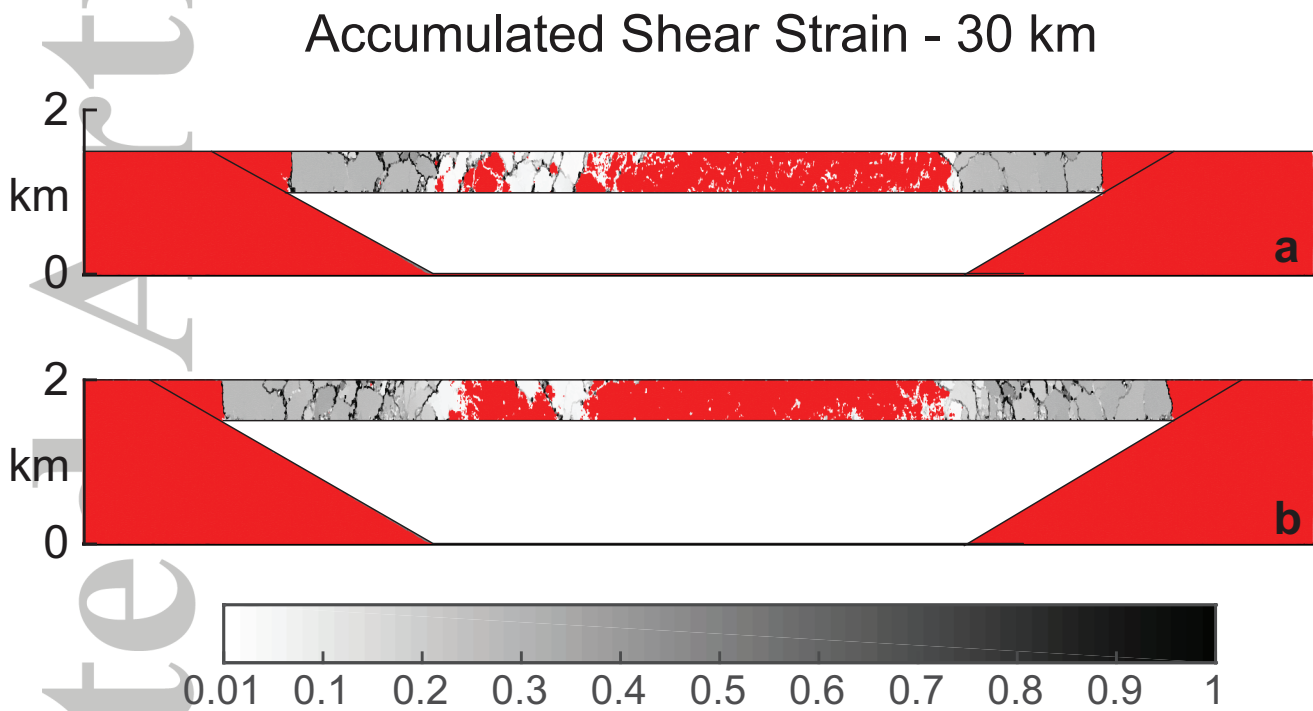


Figure 11. Total accumulated shear strain for crater diameters of 30 km and overburden thickness of 0.5 km for two difference collapsing depth: (a) 1 km and b) 1.5 km. Grey areas represent the amount of accumulated strain. Red areas represent strain-free regions interpreted as undeformed blocks. The collapsing depth does not affect the number and distribution of fractures.

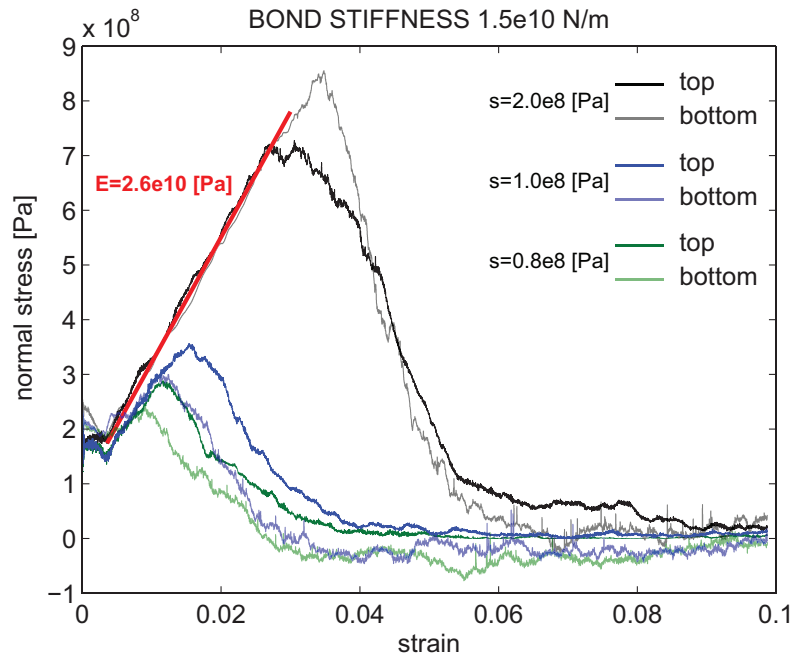


Figure 12. Stress-strain curves obtained from unconfined uniaxial compression tests at 3 different bond strengths (80, 100 and 200 MPa) of the virtual rock mass with average particles diameter of 25 m. Dark color curves refer to the top moving plane and light color curves refer to the bottom moving plane. With the red line the initial linear portions of stress-strain curves is highlighted to obtain the Young's modulus of the virtual rock mass. The bond stiffness is $1.5e10$ N/m.

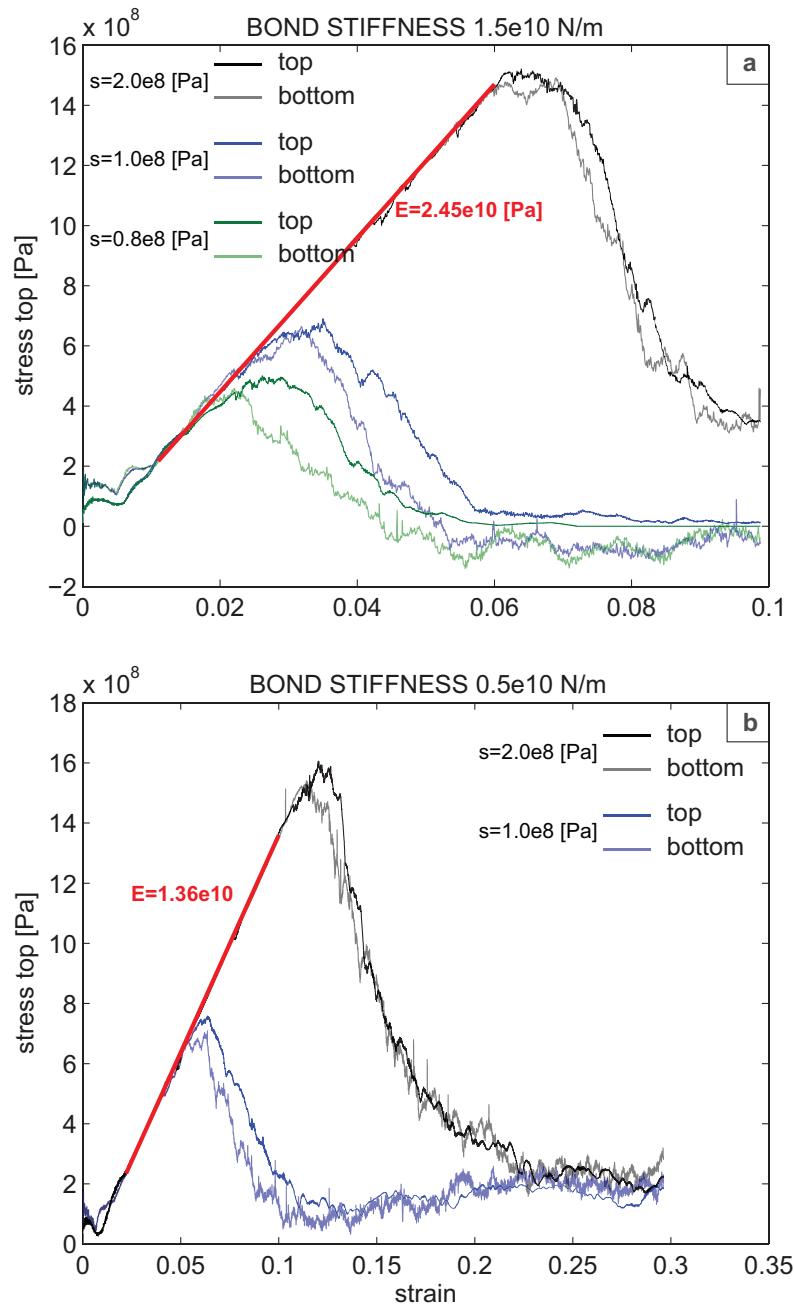


Figure 13. Stress-strain curves obtained from unconfined uniaxial compression tests at 3 different bond strengths (80, 100 and 200 MPa) and 2 different bond stiffnesses ($a=1.5e10$ N/m; $b=0.5e10$ N/m) of the virtual rock mass with average particles diameter of 50 m. Dark color curves refer to the top moving plane and light color curves refer to the bottom moving plane. With the red line the initial linear portions of stress-strain curves is highlighted to obtain the Young's modulus of the virtual rock mass.

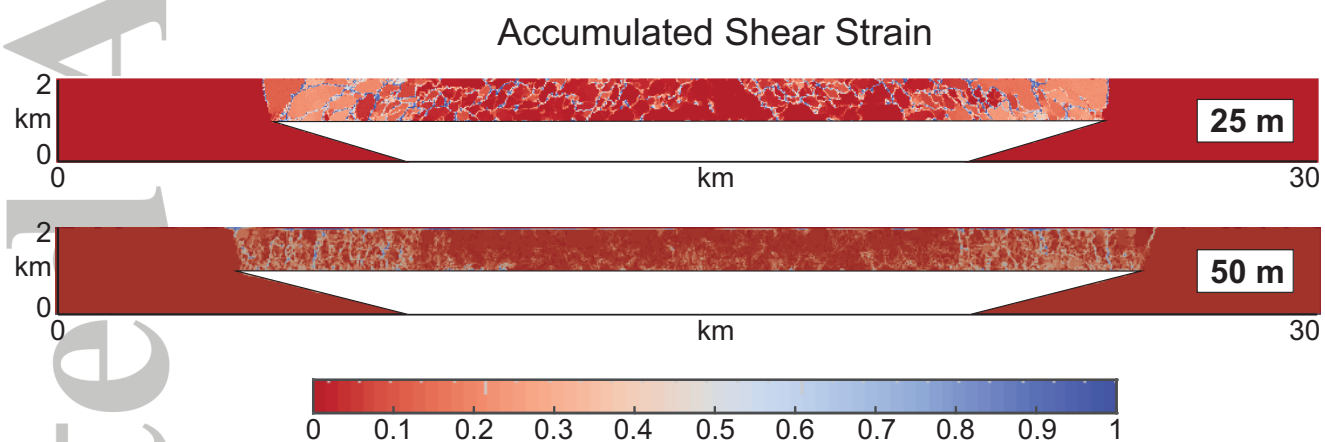


Figure 14. Total accumulated shear strain for a crater diameter of 30 km using two different average particle diameters: 25 and 50 m.

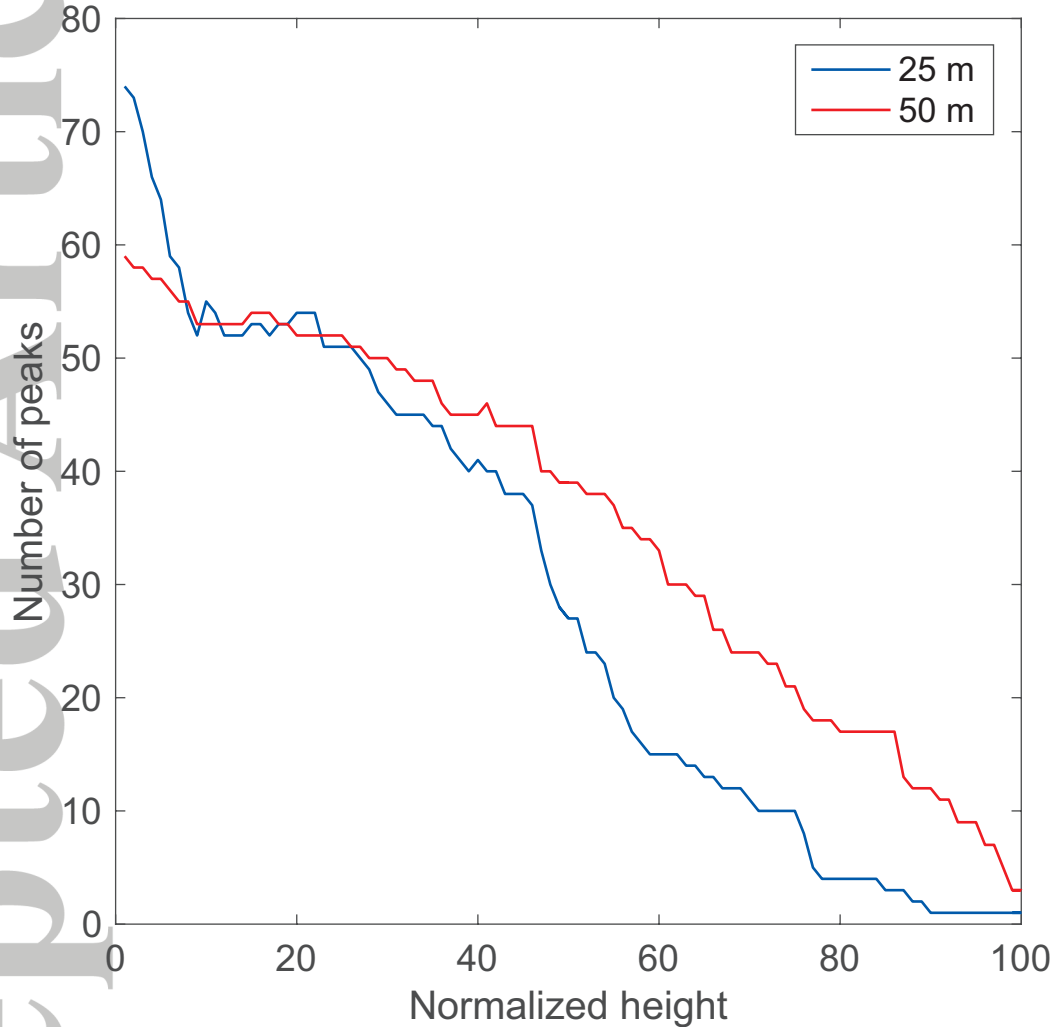


Figure 15. Number of peaks distribution as function of normalized height of topographic profile for two different average particle diameters: 25 and 50 m. Considering the differences in terms of Young's modulus and strength resulting from the calibrations, the two simulations show broadly similar distributions and total number of peaks.

Table 1. Input parameters for particles and bonds.

Parameter	Value	Unit
Max particle diameter	30	m
Min particle diameter	20	m
Particle density	2500	kg/m ³
Particle stiffness	1.5e10	N/m
Bond stiffness	1.5e10	N/m
Bond friction	0	
Bond strength	100	MPa
Poisson ratio	0.3	
Young's modulus	26	GPa

Table 2. List of simulations and setup.

Diameter (km)	Overb. thickness (km)	Collap. depth a (km)	Collap. depth b (km)
30	1	1	
	0.5	1	1.5
60	1.5	1.5	
	0.75	1.5	
120	2.25	2.25	
	1.125	2.25	
240	3	3	
	1.5	3	